

A 610-MHz survey of the ELAIS-N1 field with the Giant Metrewave Radio Telescope – Observations, data analysis and source catalogue

Timothy Garn^{*}, David A. Green, Julia M. Riley, Paul Alexander

Astrophysics Group, Cavendish Laboratory, 19 J. J. Thomson Ave., Cambridge CB3 0HE

9 November 2021

ABSTRACT

Observations of the ELAIS-N1 field taken at 610 MHz with the Giant Metrewave Radio Telescope are presented. Nineteen pointings were observed, covering a total area of $\sim 9 \text{ deg}^2$ with a resolution of $6 \times 5 \text{ arcsec}^2$, PA $+45^\circ$. Four of the pointings were deep observations with an rms of $\sim 40 \mu\text{Jy}$ before primary beam correction, with the remaining fifteen pointings having an rms of $\sim 70 \mu\text{Jy}$. The techniques used for data reduction and production of a mosaicked image of the region are described, and the final mosaic is presented, along with a catalogue of 2500 sources detected above 6σ . This work complements the large amount of optical and infrared data already available on the region. We calculate 610-MHz source counts down to $270 \mu\text{Jy}$, and find further evidence for the turnover in differential number counts below 1 mJy, previously seen at both 610 MHz and 1.4 GHz.

Key words: surveys – catalogues – radio continuum: galaxies

1 INTRODUCTION

The *Spitzer* Wide-area Infrared Extragalactic (SWIRE; Lonsdale et al. 2003) survey has the largest sky coverage of the legacy surveys being performed by the *Spitzer Space Telescope* (Werner et al. 2004). A total area of $\sim 49 \text{ deg}^2$ of sky has been observed with the Infrared Array Camera (IRAC; Fazio et al. 2004) and Multiband Imaging Photometer for *Spitzer* (MIPS; Reike et al. 2004) instruments at 3.6, 4.5, 5.8, 8, 24, 70 and $160 \mu\text{m}$. The survey is broken down into six fields, three in the northern sky – ELAIS-N1, ELAIS-N2 and the Lockman Hole – and three in the south – ELAIS-S1, *Chandra* Deep Field South and the XMM-Large Scale Structure (XMM-LSS) field. All six regions were selected to be away from the Galactic disk, in order to minimize background cirrus emission.

There is a large amount of multi-wavelength information available on all six SWIRE fields. The three ELAIS fields were observed as part of the European Large-Area *ISO* Survey (Oliver et al. 2000), which also included another northern (-N3) and southern (-S2) field. The *Infrared Space Observatory* (*ISO*) observed these regions at 6.7, 15, 90 and $175 \mu\text{m}$, and a large number of followup observations were carried out in the optical, infrared and radio bands. A band-merged catalogue, containing the *ISO* data, along with *U*, *g*^l, *r*^l, *i*^l, *Z*, *J*, *H* and *K*-band detections, and radio observations at 1.4 GHz has been produced – for more details, see Rowan-Robinson et al. (2004), and references therein.

Observations of the ELAIS-N1 region were taken with *Spitzer* in 2004 January, covering $\sim 9 \text{ deg}^2$ with the IRAC and MIPS instruments. The source catalogues have been produced,

and are available online (Surace et al. 2004), containing over 280,000 sources. The UK Infrared Deep Sky Survey (UKIDSS; Lawrence et al. 2007) intends to cover the ELAIS-N1 region in its Deep Extragalactic Survey plan, observing the full field in the *J*, *H* and *K*-bands to a depth of $K = 21$ mag. This will be a great improvement over the currently available surveys, which have a sensitivity limit of ~ 18 mag in the *K* band. Data Release 2 (Warren et al. 2007) of UKIDSS contains early shallow data on the ELAIS-N1 region. Further surveys have been carried out in the *R*-band (Fadda et al. 2004), in $H\alpha$ (Pascual et al. 2001), and with the *Chandra* X-ray telescope (Manners et al. 2003; Franceshini et al. 2005). There have been several redshift surveys of the region (Trichas et al. 2006; Berta et al. 2007), and the ELAIS-N1 region was also partially covered by the Sloan Digital Sky Survey (SDSS; Adelman-McCarty et al. 2007).

While there have been a great number of observations of the ELAIS-N1 region at optical and infrared wavelengths, there is comparatively little radio information available. The existing VLA 1.4 GHz survey of the three northern ELAIS fields (Cileigi et al. 1999), which has been included into the band-merged catalogue of Rowan-Robinson et al. (2004), reaches a 5σ limit of 0.135 mJy over 0.12 deg^2 but only a 1.15 mJy limit over its full coverage area of 4.22 deg^2 . The NVSS (Condon et al. 1998) and FIRST (Becker et al. 1995) surveys both cover the ELAIS-N1 region, but only to relatively shallow 5σ limits of 2.25 and 0.75 mJy respectively. A recent study of polarised compact sources (Taylor et al. 2007) at 1420 MHz is underway, using the Dominion Radio Astrophysical Observatory Synthesis Telescope (DRAO ST) centered on $16^{\text{h}}11^{\text{m}}00^{\text{s}}$, $+55^\circ 00' 00''$ and covering 7.4 deg^2 . The first 30 per cent of observations have been completed, with maps in

* E-mail: tsg25@cam.ac.uk

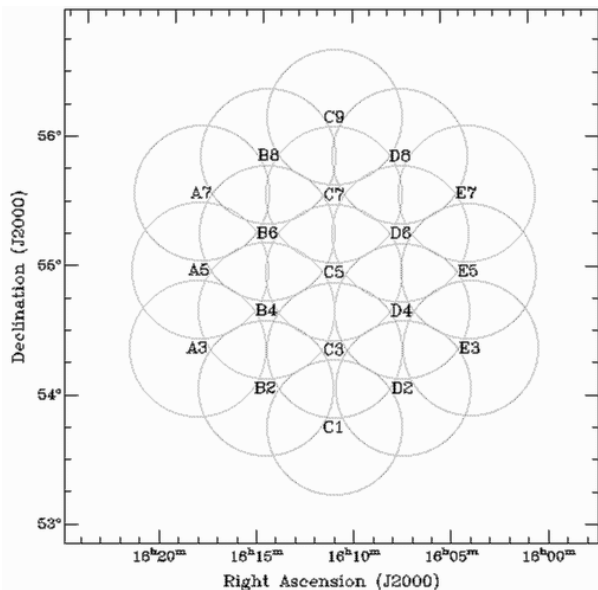


Figure 1. The 19 pointings observed in the ELAIS-N1 region. Fields B4, C3, C5 and D4 are the deep observations.

Stokes I, Q and U being produced with a maximum sensitivity of $78 \mu\text{Jy beam}^{-1}$, although with a resolution of $\sim 1 \text{ arcmin}^2$.

In order to extend the information on this region, a much larger deep radio survey is required. In this paper, we present observations of the ELAIS-N1 survey field taken at 610 MHz with the Giant Metrewave Radio Telescope (GMRT; Ananthakrishnan 2005), covering $\sim 9 \text{ deg}^2$ of sky with a resolution of $6 \times 5 \text{ arcsec}^2$, PA $+45^\circ$, centred on $16^{\text{h}}11^{\text{m}}00^{\text{s}}$, $+55^\circ00'00''$ (J2000 coordinates, which are used throughout this paper). This survey, in combination with the deep *Spitzer* data, will be used to study the infrared/radio correlation for star-forming systems (e.g. Appleton et al. 2004), and the link between the triggering of star formation and AGN activity, as well as the properties of the faint radio population at 610 MHz.

In Section 2 we describe the observations and data reduction techniques used in the creation of the survey. Section 3 presents the mosaic and a source catalogue containing 2500 sources above 6σ , along with a sample of extended sources. In Section 4 we construct the 610 MHz differential source counts, and compare them to previous works.

2 OBSERVATIONS AND DATA REDUCTION

The ELAIS-N1 region was observed for 25 hours, spread over three days in 2003 August, using the GMRT operating at 610 MHz. Nineteen pointings were observed, centred on $16^{\text{h}}11^{\text{m}}00^{\text{s}}$, $+55^\circ00'00''$ and spaced by $36'$ in a hexagonal grid (as shown in Fig. 1) in order to get nearly uniform coverage over the region. Two 16 MHz sidebands were observed, each split into 128 spectral channels, with a 16.9 s integration time.

The flux density scale was set through observations of 3C48 or 3C286, at the beginning and end of each observing session. The AIPS task SETJY was used to calculate 610 MHz flux densities of 29.4 and 21.1 Jy, respectively, using the AIPS implementation of the Baars et al. (1977) scale. Each field was observed for a series of interleaved 9 min scans in order to maximise the uv coverage, and a nearby phase calibrator, J1634+627, was observed for four minutes between every three scans to monitor any time-dependent phase

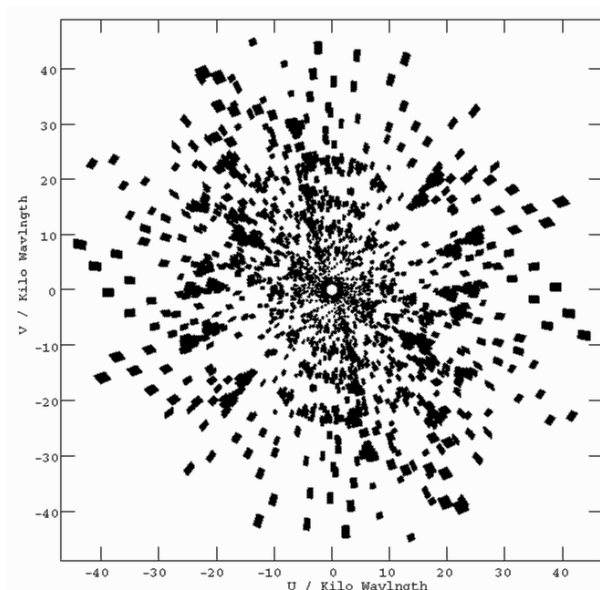


Figure 2. The uv coverage for pointing A3. Baselines less than $1 \text{ k}\lambda$ were not used in imaging and have been omitted from the figure.

and amplitude fluctuations of the telescope. The measured phase typically varied by less than 10 degrees between phase calibrator observations. Most of the fields were observed for four scans (36 mins in total), while four fields, B4, C3, C5 and D4, were observed for significantly longer, in order to give a deeper region within the main survey as there is deep optical information available on this region from UKIDSS (Warren et al. 2007). B4 and D4 were observed for 11 scans (99 mins) while C3 and C5 were observed for 12 scans (108 mins).

The imaging strategy was very similar to that used for our 610 MHz GMRT observations of the *Spitzer* extragalactic First Look Survey field (xFLS; Garn et al. 2007). An error in the timestamps of the uv data was corrected using UVFXT (for further details see Garn et al. 2007). This error is only found for observations made before the summer of 2006, and has since been fixed at the GMRT. Initial editing of the data was performed separately on each sideband with standard AIPS tasks, to remove bad baselines, antennas, and channels that were suffering from large amounts of narrow band interference, along with the first and last integration periods of each scan. The flux calibrators were used to create a bandpass correction for each antenna. In order to create a continuum channel, five central frequency channels were combined together, and an antenna-based phase and amplitude calibration created using observations of J1634+627. This calibration was applied to the original data, which was then compressed into 11 channels, each with bandwidth of 1.25 MHz (so the first few and last few spectral channels were omitted from the data, since they tended to be the noisiest). The new channel width is small enough that bandwidth smearing is not a problem in our images, and led to an effective bandwidth of 13.75 MHz in each sideband. Further flagging was performed on the 11 channel data set, and the two sidebands combined using UVFLP (again, see Garn et al. 2007) to improve the uv coverage. The coverage for one of the shallow observations is shown in Fig. 2. Baselines shorter than $1 \text{ k}\lambda$ were omitted from the imaging, since the GMRT has a large number of small baselines which would otherwise dominate the beam shape.

Each pointing was broken down into 31 smaller facets (as dis-

cussed in Garn et al. 2007), arranged in a hexagonal grid and covering an area with diameter $\sim 1^\circ 8$. These were imaged separately, each with a different assumed phase centre. The large area covered (compared with the Full-Width Half-Maximum of the GMRT, which is $\sim 0^\circ 74$) allows bright sources well outside of the observed region to be cleaned from the images, while the faceting procedure avoids the introduction of phase errors due to the non-planar nature of the sky. All images were made with the same elliptical synthesised beam of size $6 \times 5 \text{ arcsec}^2$, position angle $+45^\circ$ by setting the parameters for the restoring beam within IMAGR. A pixel size of 1.5 arcsec was chosen, to ensure that the beam was well oversampled.

Each pointing went through three iterations of phase self-calibration at 10, 3 and 1 minute intervals, and then a final round of self-calibration correcting both phase and amplitude errors, at 10 minute intervals. The overall amplitude gain was held constant in order not to alter the flux density of sources. The self-calibration steps improved the noise level by about 10 per cent, and significantly reduced the residual sidelobes around the brighter sources.

The four deep pointings have a final rms of between 40 and 42 μJy before correction for the GMRT primary beam, while the 15 shallow fields have a noise level of between 66 and 73 μJy . These figures are very close to the expected thermal noise limits of 36 and 63 μJy respectively, calculated using

$$\sigma = \frac{\sqrt{2}T_s}{G\sqrt{n(n-1)}N_{\text{IF}}\Delta\nu\tau} \quad (1)$$

where the system temperature $T_s \approx 92 \text{ K}$, and the antenna gain $G \approx 0.32 \text{ K Jy}^{-1}$ – values taken from the GMRT website¹ – n is the number of working antennas, typically 27 during our observations, $N_{\text{IF}} = 2$ is the number of sidebands, $\Delta\nu = 13.75 \text{ MHz}$ is the effective bandwidth per sideband, and τ is the integration time for each pointing.

In Garn et al. (2007), we detected a position-dependent error with the GMRT primary beam. This led to a systematic difference between the measured flux densities of sources that were present in more than one pointing, with the fractional offset varying across the primary beam. To check for a similar effect here, we corrected each pointing for the nominal beam shape, using an 8th-order polynomial with coefficients taken from Kantharia & Rao (2001). We took the 557 sources present in the overlapping regions between two pointings with peak brightness greater than $1.5 \text{ mJy beam}^{-1}$, and looked at the fractional offsets as a function of position away from each pointing centre. Fig. 3 shows the variation in this offset with source Right Ascension. A similar trend was seen with Declination.

We repeated the analysis of Garn et al. (2007), to model the effective pointing centre of the telescope as having a systematic offset from its nominal value. By shifting the phase centre of all pointings by $\sim 2/7$ in a north-west direction before performing the primary beam correction, we were able to remove this systematic effect, as shown in Fig. 4. The amount and direction of the correction was consistent between pointings, and did not vary between the deep and shallow observations. This correction also removed the systematic effect seen in the Declination direction. The size and direction of this correction is similar to that seen in the xFLS survey.

The accuracy of the primary beam correction was then tested, as shown in Fig. 5. The fractional offset of sources in overlapping

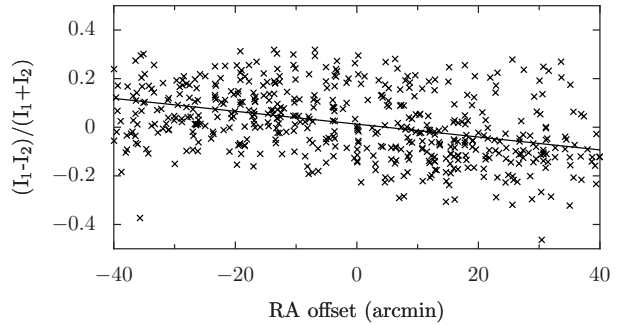


Figure 3. Fractional offset in peak brightness of all sources in overlapping regions, using the nominal primary beam centre. A gradient across the pointing is seen, leading to systematic errors in measured flux density.

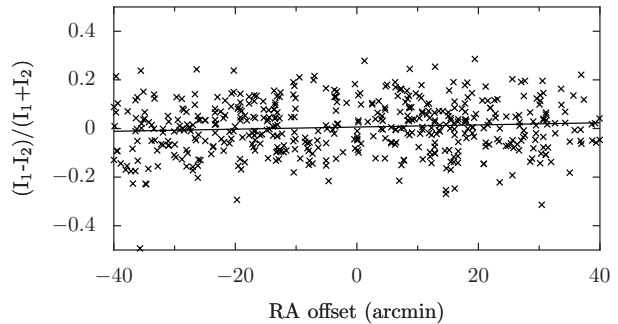


Figure 4. Fractional offset in peak brightness of sources in overlapping regions, using the shifted primary beam centre applied to all fields.

regions is now a good fit to a Gaussian, with mean of 0.009 and σ of 0.1, indicating a 10 per cent error in the absolute flux density calibration of all sources.

The 19 pointings were mosaicked together, taking into account the offset primary beam and weighting the final mosaic appropriately by the relative noise of each pointing. The mosaic was cut off at the point where the primary beam correction dropped to 20 per cent of its central value. The final mosaicked image is available via <http://www.mrao.cam.ac.uk/surveys/>.

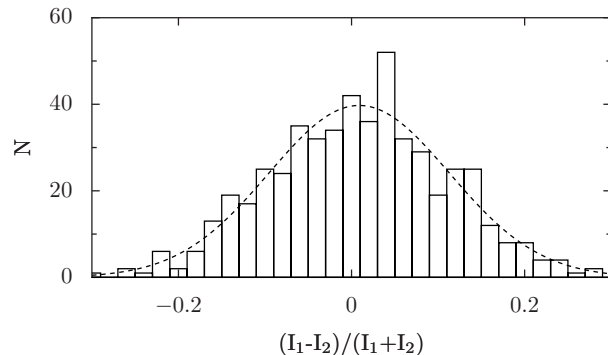


Figure 5. Distribution of fractional offsets, after correction for the shifted primary beam. The best-fit Gaussian is shown, giving a 10 per cent error in the overall flux density calibration.

¹ http://www.gmrt.ncra.tifr.res.in/gmrt_hpage/Users/Help/help.html

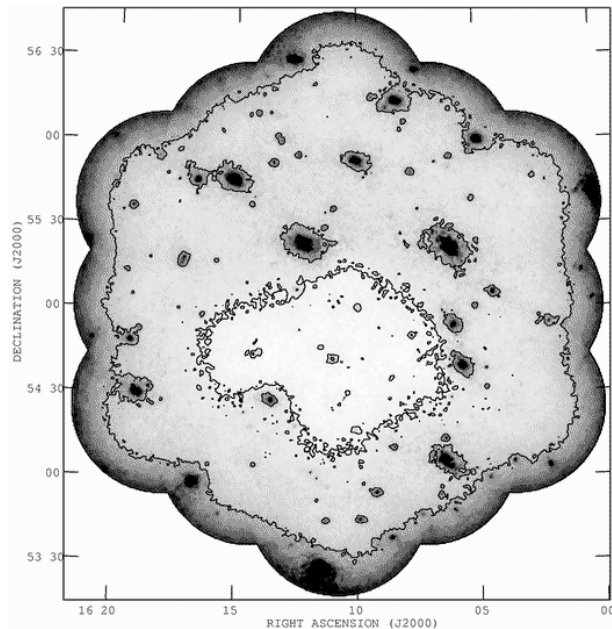


Figure 6. The rms noise of the final mosaic, calculated using Source Extractor. The grey-scale ranges between 40 and 350 μJy , and the contours are at 60 and 120 μJy respectively.

3 RESULTS AND DISCUSSION

Source Extractor (SExtractor; Bertin & Arnouts 1996) was used to calculate the rms noise σ across the mosaic. A grid of 16×16 pixels was used in order to track changes in the local noise level, which varies significantly near the brightest sources. Fig. 6 illustrates the local noise, with the grey-scale varying between 40 μJy (the noise level in the centre of the deep pointings) and 350 μJy (the noise level for the shallow pointings, at the distance where the GMRT primary beam gain was 20 per cent of its central value). The 60 and 120 μm contours are plotted, which cover the majority of the deep and shallow survey regions respectively.

A sample region of the ELAIS-N1 survey is shown in Fig. 7 to illustrate the quality of the image. Most of the sources in our survey are unresolved, although there are several with extended structures. We present a sample of these in Fig. 8.

Our GMRT data suffer from dynamic range problems near the brightest sources, and the final mosaic has increased noise and residual sidelobes in these regions. We had fewer problems with our survey of the xFLS region, due to the longer time spent on each pointing and the correspondingly better uv coverage. There were also fewer bright sources in the xFLS field, so a much smaller region was affected by residual sidelobes. Fig. 9 shows an area around one of the bright sources, to illustrate the problems caused by the residual sidelobes. While the local noise calculated by SExtractor increases due to these residuals, some of them still have an apparent signal-to-noise level that is greater than 6. We therefore opted for a two-stage selection criteria for our final catalogue.

3.1 Source fitting

An initial catalogue of 4767 sources was created using SExtractor. The mosaic was cut off at the point where the primary beam correction dropped to 20 per cent of its central value (a radius of $0^\circ 53$ from the outer pointings), however only sources inside the 30 per cent region ($0^\circ 47$) were included in the catalogue to avoid

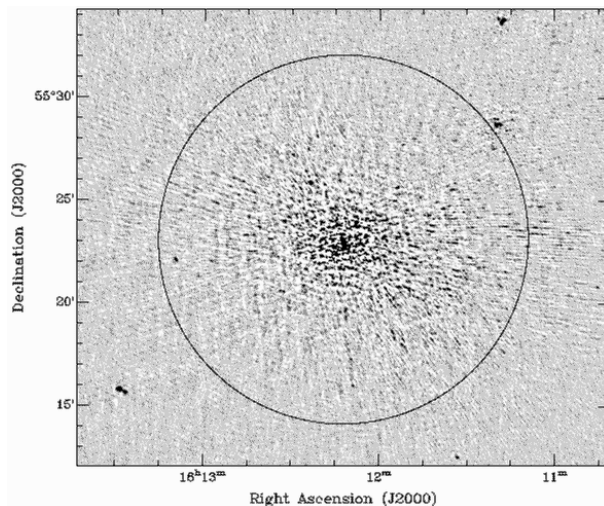


Figure 9. Source GMRTEN1 J161212.4+552308, and the errors surrounding it. The grey-scale ranges between -0.2 and 1 mJy beam^{-1} , and the source has a peak brightness of 389 mJy . The region affected by an over-density of sources is shown by the black circle, of radius 10 arcmin – see text for more details.

the mosaic edges from affecting the estimation of local noise. The requirements for a source to be included were that it had at least 5 connected pixels with brightness greater than 3σ , and a peak brightness greater than 6σ . The image pixel size meant that the beam was reasonably oversampled, so the source peak was taken to be the value of the brightest pixel within a source. The integrated flux density was calculated using the FLUX_AUTO option within SExtractor. This creates an elliptical aperture around each object (as described in Kron 1980), and integrates the flux contained within the ellipse. Comparisons between the flux density obtained through this method and through the method developed in Garn et al. (2007) – pixels above a given threshold were summed, then empirically corrected for the elliptical beam shape – give good agreement between the two techniques. Sources with Kron flux density above 1 mJy showed no statistical difference between the two flux density measurements, with an uncertainty of 3 per cent. Sources below 1 mJy had a Kron flux density that was systematically larger than the Garn et al. (2007) method by 6 per cent, with an uncertainty of 4 per cent. We chose to use the Kron method in order to avoid the empirical correction factor.

In order to estimate the area affected by artefacts near the bright sources, we calculated the number of (potentially spurious) sources in a series of concentric rings centred on a bright source, and converted this to an effective source density as a function of distance. While the noise does vary across the map, the variation is smooth and relatively slow away from the bright sources. Using the more distant rings we calculated a mean source sky density μ , and an estimate of the error in this value, σ_μ , which will be unaffected by the presence of the spurious sources, and will vary slightly between each bright central source due to the changing properties of the image.

Fig. 10 shows the source density (in arbitrary units) away from the source in Fig. 9. The clear over-density of sources can be seen within 10 arcmin of the source. If there is a significant peak in the density (greater than $\mu + 6\sigma_\mu$), then we define the size of the affected region by finding the first radius at which the source density drops below $\mu + 3\sigma_\mu$ – for this source, the affected radius is 10 arcmin. The affected region has been added to Fig. 9. Within this

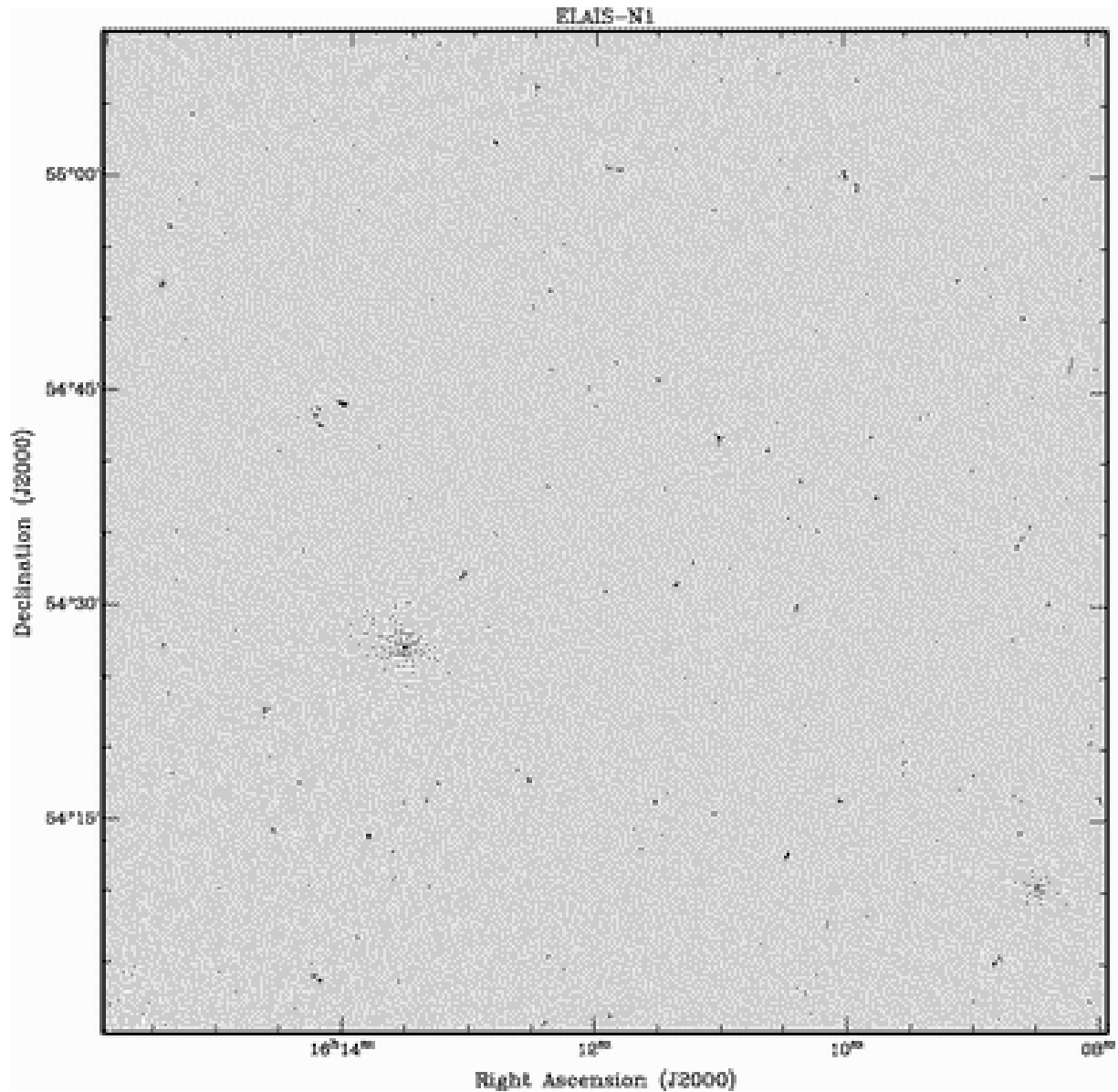


Figure 7. A 70×70 arcmin² region of the 610 MHz image, to illustrate the quality of the survey. The region is located within the deeper area of the survey, and most sources are unresolved. The grey-scale ranges between -0.2 and 1 mJy beam⁻¹, and the noise is relatively uniform and between 40 and 60 μ Jy, apart from small regions near bright sources where the noise increases.

region, only sources with a peak brightness greater than 12σ are included in our catalogue – this value was determined empirically. The source density plot for a 10 mJy source is shown in Fig. 11, on the same scale as Fig. 10 – while there may still be a slight overdensity near the centre, the increased noise level in this region, along with the 6σ cut-off reduces the risk of selecting a spurious source near sources with weak over-densities.

This analysis was repeated for all sources with a peak greater than 10 mJy in order to filter spurious sources. The final catalogue contains 2500 sources – we have erred on the side of caution in order to produce a catalogue with little contamination from spurious sources. The size of the affected region is correlated with the peak brightness of a source (with Pearson product-moment correlation coefficient of 0.53), and the number of spurious sources is also correlated with the peak brightness, with correlation coefficient 0.73 . The precise size of the affected region depends on the uv coverage

for the relevant pointing, the time spent on observations and the local noise levels.

Table 3.1 presents a sample of 60 entries in the catalogue, which is sorted by right ascension. The full table is available via <http://www.mrao.cam.ac.uk/surveys/>. Column 1 gives the IAU designation of the source, in the form GM-RTEN1 Jhhmmss.s+ddmmss, where J represents J2000.0 coordinates, hhhmmss.s represents right ascension in hours, minutes and truncated tenths of seconds, and dddmmss represents the declination in degrees, arcminutes and truncated arcseconds. Columns 2 and 3 give the right ascension and declination of the source, calculated by first moments of the relevant pixel brightnesses to give a centroid position. Column 4 gives the brightness of the peak pixel in each source, in mJy beam⁻¹, and column 5 gives the local rms noise in μ Jy beam⁻¹. Columns 6 and 7 give the integrated flux density and error, calculated from the local noise level and source

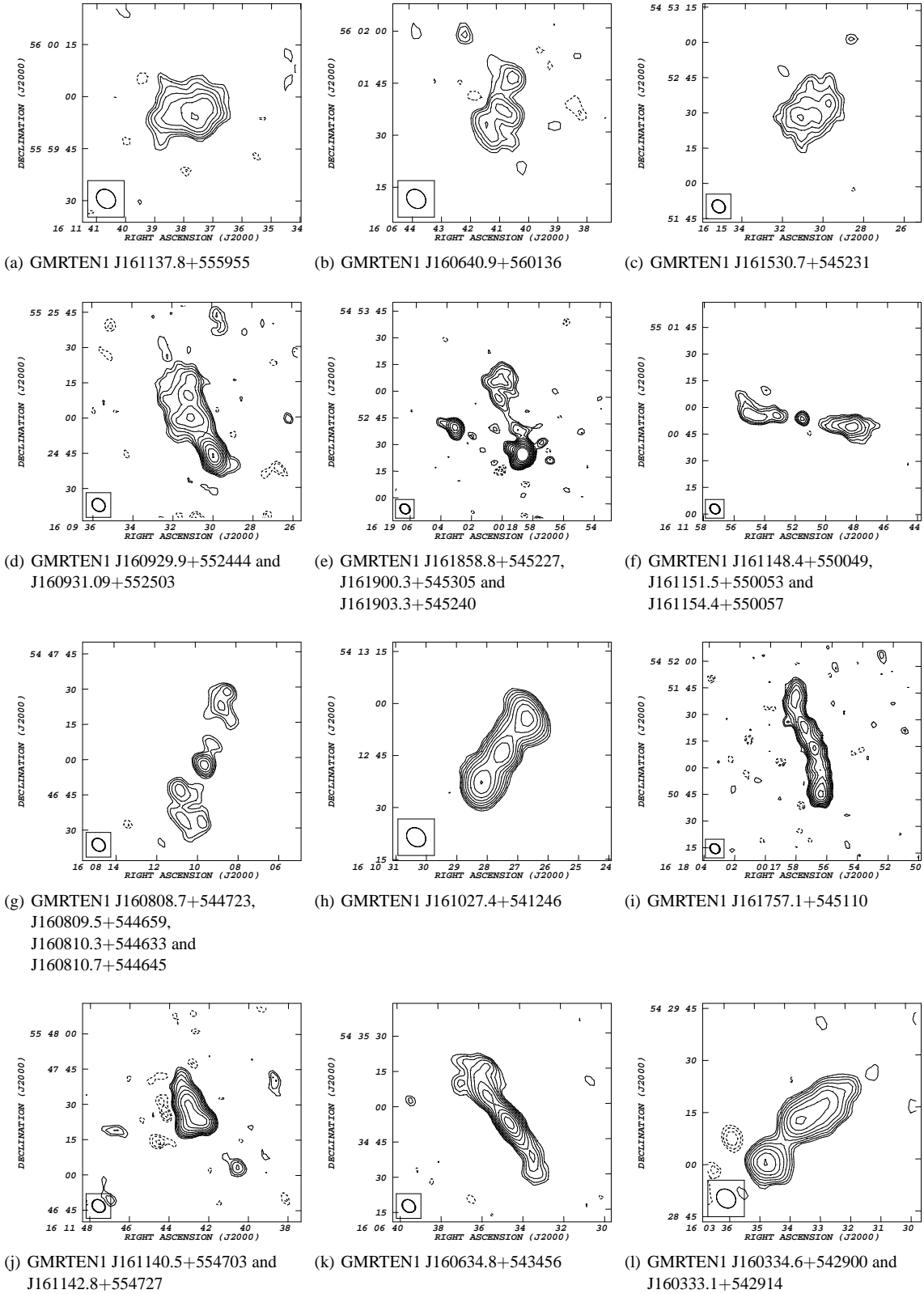


Figure 8. A selection of extended objects in the ELAIS-N1 610 MHz GMRT survey – contours are plotted at $\pm 200 \mu\text{Jy} \times 1, \sqrt{2}, 2, 2\sqrt{2}, 4, \dots$, with the exception of object (e), where the contours start at $\pm 500 \mu\text{Jy}$. Negative contours are represented by dashed lines. The resolution of the beam is shown in the bottom left of each image, and the designations of each source component are given below.

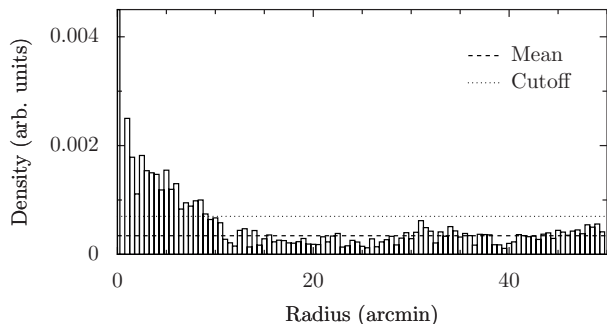


Figure 10. Density of sources, in concentric rings around the bright source shown in Fig. 9. The overdensity of sources near to the bright (389 mJy) central object can be clearly seen. The mean source density, far from the central source, is given by the large dashed line while the cutoff density defining the affected region is given by short dashes – see text for more details.

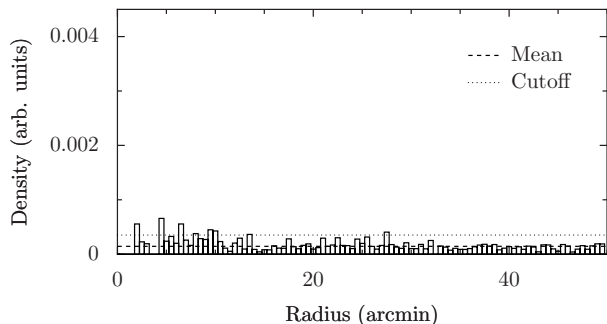


Figure 11. Density of sources, in concentric rings around a fainter (10 mJy) object in the ELAIS-N1 survey field. There is still a slight overdensity near the central source, but the signal-to-noise cutoff of 6σ ensures that spurious sources are not included in the catalogue.

size. Columns 8 and 9 give the X, Y pixel coordinates of the source centroid from the mosaic image. Column 10 is the Source Extractor deblended object flag – 1 where a nearby bright source may be affecting the calculated flux, 2 where a source has been deblended into two or more components from a single initial island of flux, and 3 when both of the above criteria apply. There are 232 sources present in our catalogue with non-zero deblend flags; it is necessary to examine the images to distinguish between the case where one extended object has been represented by two or more entries, and where two astronomically distinct objects are present.

3.2 Comparison with other surveys

In order to test the positional accuracy of our catalogue, we paired it with the 393 objects in the VLA 1.4 GHz source catalogue of Ciliegi et al. (1999), using a pairing radius of 6 arcsec. The VLA survey covers only ~ 25 per cent of our 610 MHz observations. Fig. 12 shows the position offset of the 263 matched sources compared with their VLA counterparts – the distribution of offsets is approximately Gaussian, with mean offset in Right Ascension of -0.9 arcsec, and -0.1 arcsec in Declination. The standard deviations of the distribution are 0.9 and 0.7 arcsec respectively.

We repeated this analysis with data from the FIRST survey (Becker et al. 1995). The whole of our 610 MHz survey region is covered by FIRST, and even with the reduced sensitivity of FIRST ($\sim 150 \mu\text{Jy}$ noise), 504 pairs are found within 6 arcsec.

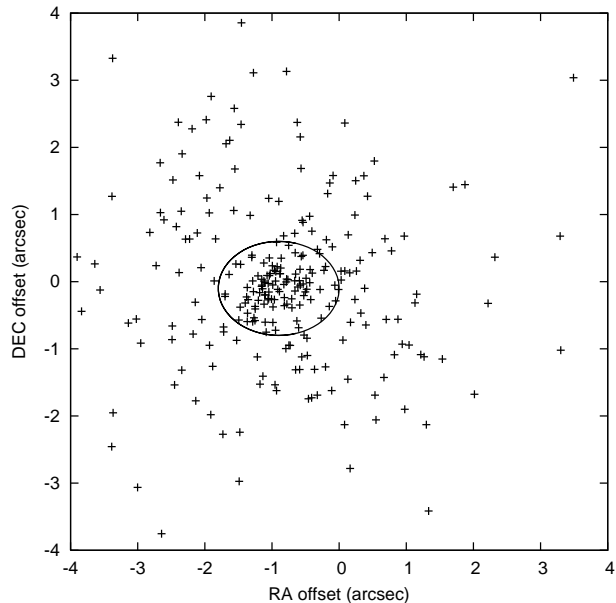


Figure 12. Source positions in the GMRT catalogue relative to the positions found in the VLA catalogue of Ciliegi et al. (1999), for unique matches within 6 arcsec. Offsets are distributed in a Gaussian fashion in RA and DEC, and the ellipse corresponding to 1σ for the distribution is shown.

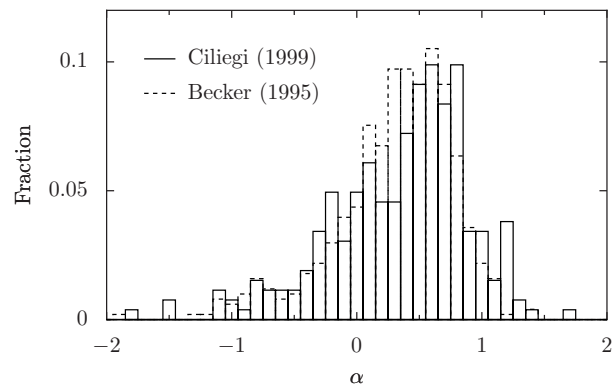


Figure 13. Radio spectral index α between 610 MHz and 1.4 GHz, for sources in the VLA ELAIS-N1 catalogue of Ciliegi et al. (solid lines) and in the FIRST catalogue (dashed lines).

We again find Gaussian-distributed position errors, with RA offset of -0.1 arcsec, standard deviation 0.4 arcsec and DEC offset of -0.1 arcsec, standard deviation 0.6 arcsec. We have not corrected the positions given in our catalogue, since it agrees closely with FIRST.

The spectral index distribution of the matched sources from both surveys is shown in Fig. 13, using the integrated flux density measurements. The distribution peaks around $\alpha = 0.7$, where α is defined such that the flux density S scales with frequency ν as $S = S_0 \nu^{-\alpha}$.

Fig. 14 shows the spectral index distribution for all sources with matches in the GMRT and FIRST catalogues (black diagonal crosses), and sources in the GMRT and Ciliegi et al. (1999) catalogues (red upright crosses). There are significant biases in Fig. 14, due to the varying sensitivity levels of the three surveys. In the region covered by Ciliegi et al. (1999), the 610 MHz completeness level is $360 \mu\text{Jy}$, shown by the black dotted line. The limiting spec-

Table 1. A sample of 60 entries from the 610-MHz ELAIS-N1 catalogue, sorted by right ascension. The full version of this table is available as Supplementary Material through the online version of this article, and via <http://www.mrao.cam.ac.uk/surveys/>.

Name	RA	Dec.	Peak	Local Noise	Int. Flux Density	Error	X	Y	Flags
(1)	J2000.0	J2000.0	mJy beam ⁻¹	μ Jy beam ⁻¹	mJy	mJy	(8)	(9)	(10)
(1)	(2)	(3)	(4)	(5)	(6)	(7)	(8)	(9)	(10)
GMRTEN1 J160319.2+542543	16:03:19.22	+54:25:43.6	0.496	75	0.415	0.067	6599	2946	0
GMRTEN1 J160319.2+553149	16:03:19.24	+55:31:49.1	0.469	66	0.383	0.054	6527	5589	0
GMRTEN1 J160319.3+554950	16:03:19.38	+55:49:50.2	0.514	85	0.265	0.054	6506	6309	0
GMRTEN1 J160320.8+550645	16:03:20.89	+55:06:45.9	2.617	97	3.425	0.175	6545	4587	0
GMRTEN1 J160321.1+553654	16:03:21.13	+55:36:54.2	0.418	69	0.309	0.076	6510	5792	0
GMRTEN1 J160322.6+554320	16:03:22.67	+55:43:20.8	0.560	75	0.444	0.068	6495	6049	0
GMRTEN1 J160323.1+543737	16:03:23.13	+54:37:37.3	1.920	74	2.256	0.119	6564	3421	0
GMRTEN1 J160324.0+550618	16:03:24.05	+55:06:18.2	0.635	84	0.495	0.079	6527	4568	0
GMRTEN1 J160326.0+540817	16:03:26.00	+54:08:17.1	0.595	94	0.486	0.081	6579	2248	0
GMRTEN1 J160327.7+552647	16:03:27.78	+55:26:47.3	3.240	84	3.867	0.149	6484	5387	0
GMRTEN1 J160327.9+543326	16:03:27.99	+54:33:26.0	0.452	75	0.338	0.064	6540	3253	0
GMRTEN1 J160329.5+540705	16:03:29.55	+54:07:05.7	0.869	131	0.681	0.117	6559	2200	0
GMRTEN1 J160330.8+542454	16:03:30.83	+54:24:54.3	0.483	78	0.837	0.097	6533	2912	0
GMRTEN1 J160331.1+554327	16:03:31.14	+55:43:27.2	0.473	76	0.555	0.071	6447	6052	0
GMRTEN1 J160331.3+545000	16:03:31.39	+54:50:00.7	0.408	67	0.322	0.055	6503	3916	0
GMRTEN1 J160332.3+553000	16:03:32.38	+55:30:00.2	0.508	69	0.536	0.076	6454	5514	0
GMRTEN1 J160332.6+554622	16:03:32.66	+55:46:22.6	3.212	76	4.152	0.153	6435	6169	0
GMRTEN1 J160332.9+541746	16:03:32.90	+54:17:46.8	0.474	73	0.381	0.060	6528	2627	0
GMRTEN1 J160333.1+542914	16:03:33.11	+54:29:14.2	2.377	73	9.697	0.226	6515	3085	3
GMRTEN1 J160333.6+552623	16:03:33.69	+55:26:23.7	0.773	78	0.878	0.101	6451	5370	0
GMRTEN1 J160333.7+540540	16:03:33.70	+54:05:40.6	7.541	294	9.799	0.552	6536	2142	0
GMRTEN1 J160334.6+542900	16:03:34.68	+54:29:00.2	2.326	80	4.235	0.167	6506	3075	3
GMRTEN1 J160335.1+551534	16:03:35.19	+55:15:34.1	0.462	74	0.333	0.066	6454	4937	0
GMRTEN1 J160335.2+555419	16:03:35.24	+55:54:19.5	0.762	105	0.984	0.108	6412	6486	0
GMRTEN1 J160335.2+540515	16:03:35.25	+54:05:15.3	38.494	383	50.351	0.961	6528	2125	0
GMRTEN1 J160336.5+555147	16:03:36.55	+55:51:47.5	0.500	79	0.662	0.082	6408	6385	0
GMRTEN1 J160336.9+544120	16:03:36.90	+54:41:20.7	0.532	68	0.853	0.092	6480	3568	0
GMRTEN1 J160337.6+545944	16:03:37.64	+54:59:44.2	0.547	80	0.530	0.077	6457	4303	0
GMRTEN1 J160338.7+554348	16:03:38.77	+55:43:48.1	0.771	80	1.743	0.135	6404	6065	0
GMRTEN1 J160339.0+545943	16:03:39.05	+54:59:43.8	0.500	80	0.415	0.065	6449	4303	0
GMRTEN1 J160339.3+551352	16:03:39.37	+55:13:52.0	0.516	78	0.414	0.063	6432	4868	0
GMRTEN1 J160339.6+542953	16:03:39.68	+54:29:53.2	0.701	66	0.647	0.078	6476	3110	0
GMRTEN1 J160339.7+550600	16:03:39.75	+55:06:00.4	0.584	80	0.418	0.069	6438	4554	0
GMRTEN1 J160340.1+545127	16:03:40.10	+54:51:27.4	0.711	79	0.639	0.079	6451	3972	0
GMRTEN1 J160340.1+550544	16:03:40.15	+55:05:44.9	0.495	81	0.392	0.069	6436	4543	0
GMRTEN1 J160340.8+554325	16:03:40.83	+55:43:25.8	1.447	81	4.633	0.210	6392	6050	0
GMRTEN1 J160341.2+552611	16:03:41.27	+55:26:11.8	0.475	68	0.460	0.065	6408	5361	0
GMRTEN1 J160341.5+552205	16:03:41.59	+55:22:05.4	0.638	69	0.614	0.080	6411	5197	0
GMRTEN1 J160341.6+553203	16:03:41.66	+55:32:03.4	0.462	69	0.365	0.062	6400	5595	0
GMRTEN1 J160343.1+540324	16:03:43.13	+54:03:24.6	0.908	126	0.556	0.092	6483	2050	0
GMRTEN1 J160344.8+540320	16:03:44.84	+54:03:20.4	1.168	118	0.856	0.110	6473	2047	0
GMRTEN1 J160345.8+553021	16:03:45.84	+55:30:21.4	0.381	60	0.370	0.065	6378	5527	0
GMRTEN1 J160345.8+554238	16:03:45.88	+55:42:38.3	0.653	76	2.566	0.156	6365	6018	0
GMRTEN1 J160346.5+552855	16:03:46.56	+55:28:55.8	0.577	73	0.510	0.076	6375	5469	0
GMRTEN1 J160346.6+550826	16:03:46.62	+55:08:26.0	0.525	70	0.416	0.065	6396	4650	0
GMRTEN1 J160348.3+542626	16:03:48.37	+54:26:26.4	2.328	80	2.660	0.133	6429	2970	0
GMRTEN1 J160348.6+550124	16:03:48.61	+55:01:24.3	0.477	78	0.257	0.050	6392	4368	0
GMRTEN1 J160349.2+554243	16:03:49.21	+55:42:43.9	3.349	85	4.224	0.163	6346	6021	0
GMRTEN1 J160350.0+545634	16:03:50.06	+54:56:34.6	0.435	67	0.371	0.058	6389	4175	0
GMRTEN1 J160350.4+550717	16:03:50.43	+55:07:17.2	0.597	78	0.626	0.083	6376	4603	0
GMRTEN1 J160350.5+541302	16:03:50.51	+54:13:02.7	0.770	80	0.535	0.068	6430	2435	0
GMRTEN1 J160351.1+555644	16:03:51.13	+55:56:44.4	3.996	120	7.391	0.287	6321	6581	0
GMRTEN1 J160351.2+552346	16:03:51.24	+55:23:46.1	0.519	80	0.640	0.072	6354	5262	0
GMRTEN1 J160351.3+540609	16:03:51.38	+54:06:09.9	0.951	110	0.843	0.110	6432	2159	0
GMRTEN1 J160352.6+550012	16:03:52.62	+55:00:12.8	0.510	71	0.592	0.076	6370	4320	0
GMRTEN1 J160352.8+542943	16:03:52.80	+54:29:43.5	2.258	82	2.422	0.124	6400	3101	0
GMRTEN1 J160353.2+550309	16:03:53.29	+55:03:09.9	0.570	74	0.500	0.072	6363	4438	0
GMRTEN1 J160355.5+553844	16:03:55.52	+55:38:44.9	0.463	73	0.242	0.050	6314	5861	0
GMRTEN1 J160356.2+550126	16:03:56.20	+55:01:26.7	0.472	77	0.380	0.063	6348	4369	0
GMRTEN1 J160356.2+550415	16:03:56.25	+55:04:15.3	0.506	83	0.451	0.068	6345	4481	0

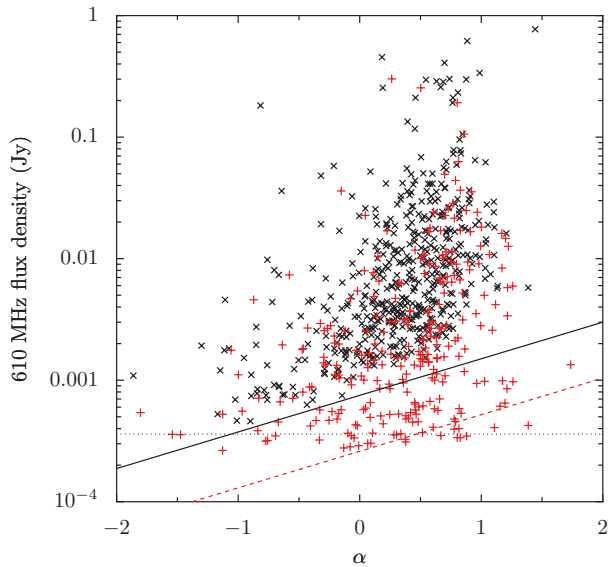


Figure 14. The variation in spectral index α with 610 MHz flux density. Black diagonal crosses represent sources in the GMRT and FIRST catalogues, with the solid black line showing the limiting spectral index that could be detected, given the respective sensitivity levels. Red upright crosses represent sources in the corresponding GMRT and Ciliegi et al. catalogues, with the dashed red line showing the limit on α . The 610 MHz flux density limit is shown by the dotted black line.

tral indices for sources at the sensitivity levels of the 1.4 GHz surveys are shown (FIRST – solid black line, Ciliegi – dashed red line). In order to look for variations in the source population, we calculate the mean and median spectral indices for sources with detections in the Ciliegi catalogue, with 610 MHz flux density between $500 \mu\text{Jy}$ and 1 mJy – the point at which the turnover in source counts becomes visible (see Section 4) – and above 1 mJy. The mean values of α are 0.22 ± 0.09 and 0.45 ± 0.04 respectively, and the median values are 0.36 ± 0.12 and 0.56 ± 0.04 . There are 48 and 168 sources in the two flux density bins. The bias against steep-spectrum sources at low flux densities (which is visible in Fig. 14) means that, for a source with 610 MHz flux density of $500 \mu\text{Jy}$, the largest value of α that would be detectable is ~ 0.8 and so this apparent flattening at fainter flux densities may simply be due to sample bias. However, Bondi et al. (2007) also find significantly flatter spectral indices for fainter radio sources, again comparing 610 MHz and 1.4 GHz data, and attribute this to the emergence of a population of low-luminosity AGNs – see Section 4 for more details.

4 DIFFERENTIAL SOURCE COUNTS

We derived source counts for the ELAIS-N1 field by considering two separate regions of the map. In order to study the 610 MHz source counts at low flux densities, we selected a $70 \times 70 \text{ arcmin}^2$ region (shown in Fig. 7), which was free from spurious sources above the local 6σ value. The region comes from the deeper section of the survey field. Fig. 15 shows the distribution of pixel noise levels (taken from the SExtractor rms map), along with the cumulative fraction of pixels with noise below a given flux density.

We constructed source counts by binning our sources by their integrated flux density, with bins ranging between $270 \mu\text{Jy}$ and 10 mJy. The lower limit was selected as the 6σ flux density cor-

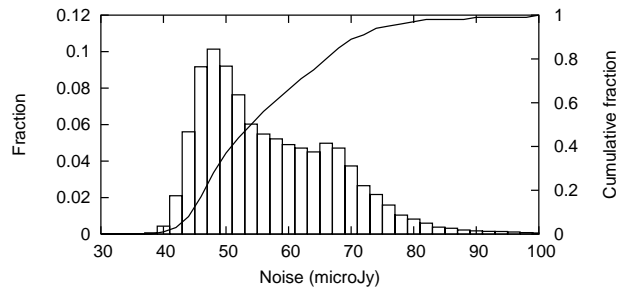


Figure 15. The fraction of pixels in the $70 \times 70 \text{ arcmin}^2$ region of the SExtractor rms map with each noise level (boxes, and left-hand axis), along with the cumulative fraction of pixels with noise below a particular value (solid line, and right-hand axis).

responding to a noise of $45 \mu\text{Jy}$, close to the peak in noise distribution seen in Fig. 15. We selected a relatively low upper limit of 10 mJy, since our region was specifically chosen for its lack of brighter sources (and the errors resulting from these sources).

The source counts were corrected for the fraction of the image over which they could be detected, taking into account the increase in noise near the bright sources, and for the resolution bias inherent in constructing flux density counts from a catalogue with a signal-to-noise ratio based around the peak brightness of a source. We use the resolution corrections of Moss et al. (2007), who found that ~ 7 per cent of sources below $360 \mu\text{Jy}$ and 3 per cent of sources between 360 and $1000 \mu\text{Jy}$ were missed from a similar resolution GMRT 610 MHz survey of the *XMM-Newton/Chandra* survey field. No correction for Eddington bias has been made, since Moss et al. (2007) find that it only affects their faintest flux density bin, increasing it by approximately 20 per cent.

The differential source count dN/dS was calculated by dividing N_c , the corrected number of sources in each bin, by $A\Delta S$, where A is the total area of the image in steradians, and ΔS is the width of the flux bin in Jy, i.e.

$$\frac{dN}{dS} = \frac{N_c}{A\Delta S} \quad (2)$$

We calculated the differential source count for sources with flux densities above 10 mJy by considering the central $\sim 4 \text{ deg}^2$ of the map. This region has several bright sources with residual side-lobes, but inspection of these residuals found them to have typical flux densities of below 1 mJy, which will therefore not affect the bright source counts. No corrections for resolution bias or Eddington bias have been made for these brighter sources.

Table 4 gives the source counts, mean flux density $\langle S \rangle$ of sources in each bin, dN/dS and dN/dS normalised by $\langle S \rangle^{2.5}$, the value expected from a static Euclidean universe. dN/dS is plotted in Fig. 16, along with 610 MHz source counts from further GMRT surveys of the *XMM-Newton/Chandra* survey field (Moss et al. 2007), the VVDS-VLA Deep Field (Bondi et al. 2007), and our previous survey of the xFLS field (Garn et al. 2007). A series of Westerbork Synthesis Radio Telescope (WSRT) surveys at 610 MHz (by Valentijn et al. 1977; Katgert 1979; Valentijn 1980; Katgert-Merkelijn et al. 1985) are also shown for comparison.

Fig. 17 shows the normalised differential source counts. There is good agreement in the various surveys above 1 mJy, and all surveys show a turnover just above 1 mJy although there is approximately a factor of 2 discrepancy between the highest and lowest points in the value of $dN/dS \langle S \rangle^{2.5}$ below this flux density. A variation in source counts has been previously observed at 1.4 GHz (see e.g. Seymour et al. 2004; Huynh et al. 2005; Biggs & Ivison 2006).

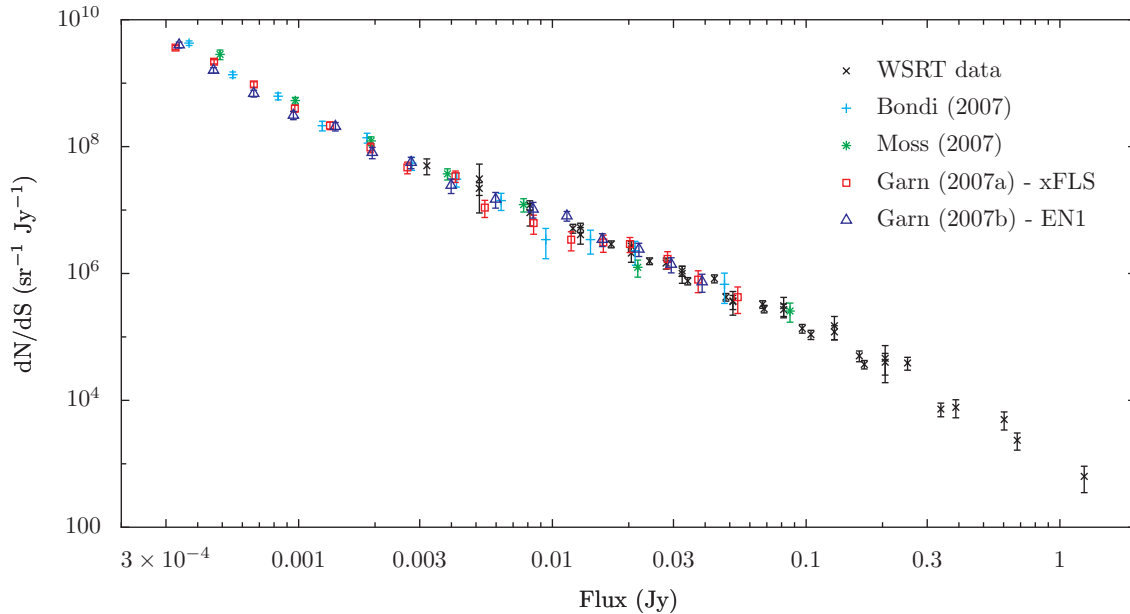


Figure 16. Differential source counts $\frac{dN}{dS}$ at 610 MHz from surveys taken with the WSRT (Valentijn et al. 1977; Katgert 1979; Valentijn 1980; Katgert-Merkelijn et al. 1985) and GMRT (Bondi et al. 2007; Moss et al. 2007; Garn et al. 2007)

Table 2. 610 MHz differential source counts for the ELAIS-N1 survey.

Flux Bin (mJy)	$\langle S \rangle$ (mJy)	N	N_c	dN/dS ($\text{sr}^{-1} \text{Jy}^{-1}$)	$dN/dS \langle S \rangle^{2.5}$ ($\text{sr}^{-1} \text{Jy}^{1.5}$)
0.270 – 0.387	0.380	89	195.9	$4.0 \pm 0.4 \times 10^9$	8.44 ± 0.89
0.387 – 0.556	0.462	100	111.9	$1.6 \pm 0.2 \times 10^9$	7.34 ± 0.73
0.556 – 0.798	0.665	67	69.2	$6.9 \pm 0.8 \times 10^8$	7.87 ± 0.96
0.798 – 1.145	0.953	45	45.0	$3.1 \pm 0.5 \times 10^8$	8.77 ± 1.31
1.145 – 1.643	1.396	43	43.0	$2.1 \pm 0.3 \times 10^8$	15.2 ± 2.31
1.643 – 2.358	1.950	24	24.0	$8.1 \pm 1.6 \times 10^7$	13.6 ± 2.77
2.358 – 3.384	2.775	24	24.0	$5.6 \pm 1.2 \times 10^7$	22.9 ± 4.67
3.384 – 4.856	3.989	15	15.0	$2.4 \pm 0.6 \times 10^7$	24.7 ± 6.37
4.856 – 6.968	5.971	13	13.0	$1.5 \pm 0.4 \times 10^7$	40.9 ± 11.3
6.968 – 10.00	8.394	13	13.0	$1.0 \pm 0.3 \times 10^7$	66.7 ± 18.5
10.00 – 13.49	11.41	33	22.0	$8.1 \pm 1.4 \times 10^6$	112 ± 19.6
13.49 – 18.20	15.73	19	19.0	$3.4 \pm 0.8 \times 10^6$	107 ± 24.6
18.20 – 24.56	21.93	18	18.0	$2.4 \pm 0.6 \times 10^6$	173 ± 40.6
24.56 – 33.14	29.41	14	14.0	$1.4 \pm 0.4 \times 10^6$	207 ± 55.3
33.14 – 44.72	38.92	10	10.0	$7.4 \pm 0.2 \times 10^5$	221 ± 69.8
44.72 – 60.34	53.74	2	2.0	$1.1 \pm 0.1 \times 10^5$	73.3 ± 51.9
60.34 – 81.41	68.60	3	3.0	$1.2 \pm 0.7 \times 10^5$	150.1 ± 86.7
81.41 – 109.8	00.00	0	0.0	0.0	0.0
109.8 – 148.2	134.0	1	1.0	$2.2 \pm 2.2 \times 10^4$	147 ± 147
148.2 – 200.0	191.9	1	1.0	$1.7 \pm 1.7 \times 10^4$	267 ± 267

In particular, Biggs & Ivison (2006) and Simpson et al. (2006) find a factor of 2 difference in the 1.4 GHz source counts for different fields at $\sim 180 \mu\text{Jy}$, equivalent to $\sim 350 \mu\text{Jy}$ at 610 MHz for an assumed spectral index of 0.8. This difference could be due to cosmic variance and the small numbers of sources detected in each field at these depths, and further data is needed to determine where the true source counts lie at these flux density levels.

The turnover in source counts is a well-known feature of the source counts at 1.4 GHz, and is thought to be due to the emergence of a new population of sources, with some authors (e.g. Condon 1989; Rowan-Robinson et al. 1993; Hopkins et al. 1998; Seymour et al. 2004) attributing it to star-forming galaxies, while

others (Jarvis & Rawlings 2004; Simpson et al. 2006) claiming that low-luminosity AGNs may form an important contribution to the source counts at these levels. The turnover occurs at 1 mJy at 1.4 GHz, equivalent to ~ 1.9 mJy at 610 MHz for a spectral index of 0.8, which is consistent with Fig. 17.

In Fig. 18 we show the differential source counts from the combination of our ELAIS-N1 and *Spitzer* extragalactic First Look Survey field – there are more than a hundred sources in the lowest four flux bins, leading to the most precise estimation of the 610 MHz source counts to date.

ACKNOWLEDGEMENTS

We thank the staff of the GMRT who have made these observations possible. TG thanks the UK STFC for a Studentship. The GMRT is operated by the National Centre for Radio Astrophysics of the Tata Institute of Fundamental Research, India.

REFERENCES

- Adelman-McCarty J. K., et al., 2007, astro-ph/0707.3413
- Ananthakrishnan S., 2005, Proc. 29th Int. Cos. Ray Conf., 10, 125
- Appleton P. N., et al., 2004, ApJS, 154, 147
- Baars J., Genzel R., Pauliny-Toth I., Witzel A., 1977, A&A, 61, 99
- Becker R. H., White R. L., Helfand D. J., 1995, ApJ, 450, 559
- Berta S., et al., 2007, A&A, 467, 565
- Bertin E., Arnouts S., 1996, A&AS, 117, 393
- Biggs A. D., Ivison R. J., 2006, MNRAS, 371, 963
- Bondi M., et al., 2007, A&A, 463, 519
- Ciliegi P., et al., 1999, MNRAS, 302, 222
- Condon J. J., 1989, ApJ, 338, 13
- Condon J. J., Cotton W. D., Yin Q. F., Perley R. A., Taylor G. B., Broderick G. B., 1998, AJ, 115, 1693

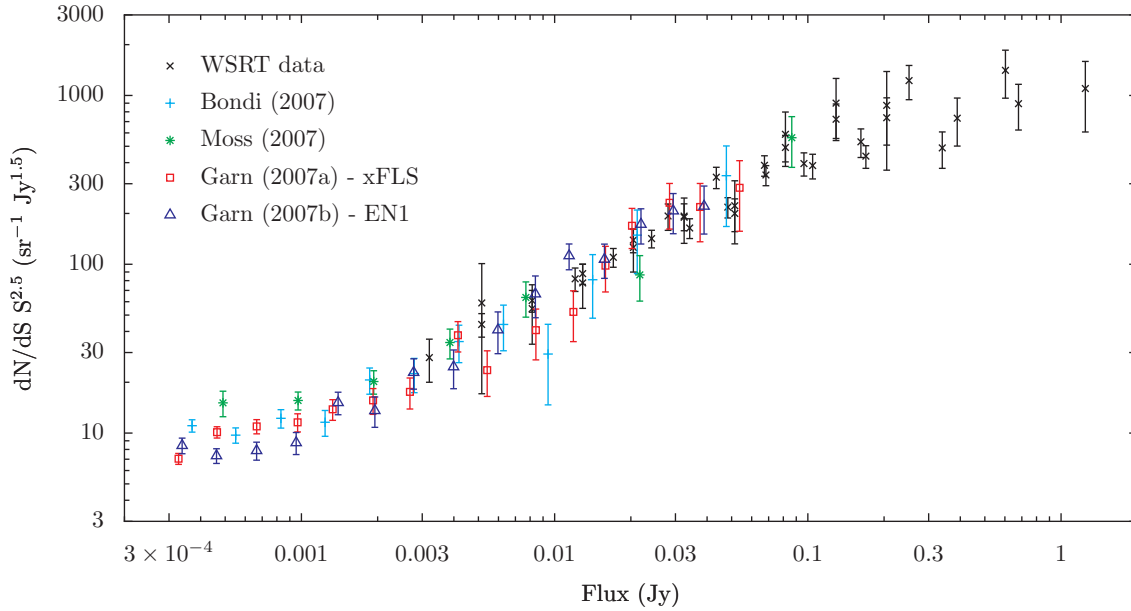


Figure 17. Differential source counts at 610 MHz (Valentijn et al. 1977; Katgert 1979; Valentijn 1980; Katgert-Merkelijn et al. 1985; Bondi et al. 2007; Moss et al. 2007; Garn et al. 2007), normalised by the value expected in a static Euclidean universe. The turnover in source counts is visible around 1 mJy, although there is considerable scatter in the various data sets below this flux density.

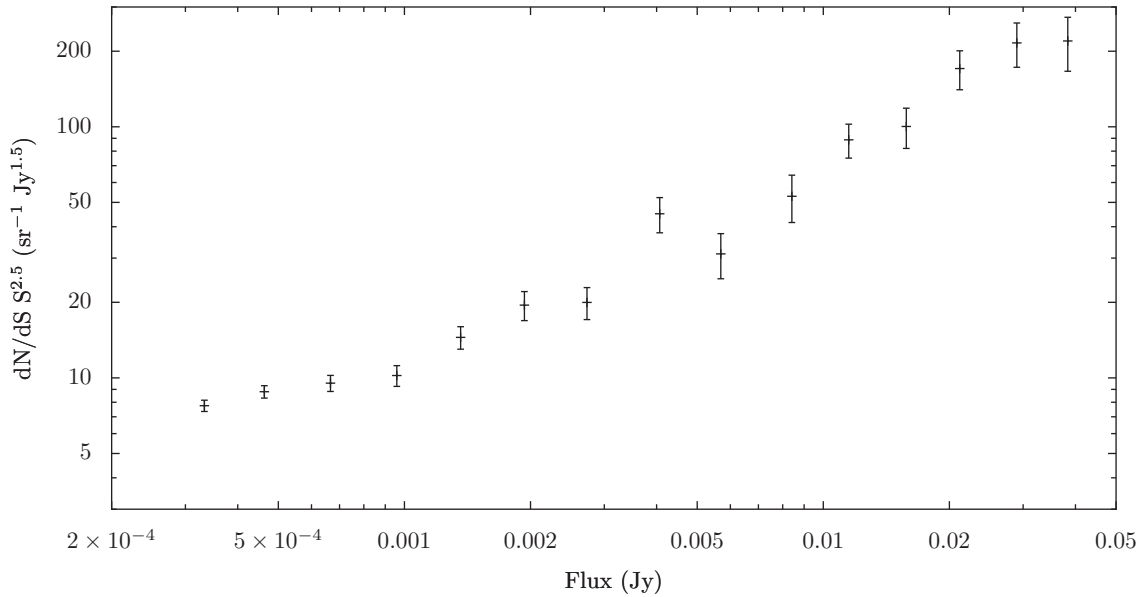


Figure 18. The normalised 610 MHz differential source counts, found by combining this work and the xFLS survey of Garn et al. (2007).

Fadda D., Jannuzi B. T., Ford A., Storrie-Lombardi L. J., 2004, *AJ*, 128, 1
Fazio G., et al., 2004, *ApJS*, 154, 10
Franceshini A., et al., 2005, *AJ*, 129, 2074
Garn T., Green D. A., Hales S. E. G., Riley J. M., Alexander P., 2007, *MNRAS*, 376, 1251
Hopkins A. M., Mobasher B., Cram L., Rowan-Robinson M., 1998, *MNRAS*, 296, 839
Huynh M. T., Jackson C. A., Norris R. P., Prandoni I., 2005, *AJ*, 130, 1373
Jarvis M. J., Rawlings S., 2004, *New Astron. Rev.*, 48, 1173
Kantharia N., Rao A., 2001, GMRT Technical Note R00185

Katgert J. K., 1979, *A&A*, 73, 107
Katgert-Merkelijn J. K., Windhorst R. A., Katgert P., Robertson J. G., 1985, *A&AS*, 61, 517
Kron R. G., 1980, *ApJSS*, 43, 305
Lawrence A., et al., 2007, *MNRAS*, 379, 1599
Lonsdale C., et al., 2003, *PASP*, 115, 897
Manners J. C., et al., 2003, *MNRAS*, 343, 293
Moss D., Seymour N., McHardy I. M., Dwelly T., Page M. J., Loaring N. S., 2007, *MNRAS*, 378, 995
Oliver S., et al., 2000, *MNRAS*, 316, 749
Pascual S., Gallego J., Aragón-Salamanca A., Zamorano J., 2001, *A&A*, 379, 798

- Reike G., et al., 2004, *ApJS*, 154, 25
- Rowan-Robinson M., Benn C. R., Lawrence A., McMahon R. G., Broadhurst T. J., 1993, *MNRAS*, 263, 123
- Rowan-Robinson M., et al., 2004, *MNRAS*, 351, 1290
- Seymour N., McHardy I. M., Gunn K. F., 2004, *MNRAS*, 352, 131
- Simpson C., et al., 2006, *MNRAS*, 372, 741
- Surace J. A., et al., 2004, *SWIRE ELAIS N1 Source Catalogs*, Online data
- Taylor A. R., et al., 2007, *ApJ*, 666, 201
- Trichas M., Rowan-Robinson M., Waddington I., Babbedge T. S. R., 2006, *Studying Galaxy Evolution with Spitzer and Herschel*, CUP Conference Series
- Valentijn A. E., 1980, *A&A*, 89, 234
- Valentijn E. A., Jaffe W. J., Perola G. C., 1977, *A&A*, 28, 333
- Warren S. J., et al., 2007, *astro-ph/0703037v2*
- Werner M., et al., 2004, *ApJS*, 154, 1